Influence of nutrient availability and quorum sensing on the formation of metabolically inactive microcolonies within structurally heterogeneous bacterial biofilms: An individual-based 3D cellular automata model

Lakshmi Machineni, Anil Rajapantul, Vandana Nandamuri, Parag D. Pawar
Department of Chemical Engineering, Indian Institute of Technology Hyderabad, India

Corresponding Author
Parag D. Pawar
Department of Chemical Engineering
Indian Institute of Technology Hyderabad
Medak, Telangana 502 205, India
Tel.: +91 40 2301 6068
Fax: +91 40 2301 6032
Email: parag@iith.ac.in

Keywords: biofilms; heterogeneity; metabolic diversity; quorum sensing; autoinducer; extracellular polymeric substances

Abstract

The resistance of bacterial biofilms to antibiotic treatment has been attributed to the emergence of structurally heterogeneous microenvironments containing metabolically inactive cell populations. In this study, we use a three-dimensional individual-based cellular automata model to investigate the influence of nutrient availability and quorum sensing on microbial heterogeneity in growing biofilms. Mature biofilms exhibited at least three structurally distinct strata: a high-volume, homogeneous region sandwiched between two compact sections of high heterogeneity. Cell death occurred preferentially in layers in close proximity to the substratum, resulting in increased heterogeneity in this section of the biofilm; the thickness and heterogeneity of this lowermost layer increased with time, ultimately leading to sloughing. The model predicted the formation of metabolically dormant cellular microniches embedded within faster growing cell clusters. Biofilms utilizing quorum sensing were more heterogeneous compared to their non-quorum sensing counterparts, and resisted sloughing, featuring a cell-devoid layer of EPS atop the substratum upon which the remainder of the biofilm developed. Overall, our study provides a computational framework to analyze metabolic diversity and heterogeneity of biofilm-associated microorganisms, and may pave the way towards gaining further insights into the biophysical mechanisms of antibiotic resistance.

Introduction

Although microorganisms have been traditionally investigated as single-cell, planktonic entities, analyses of bacterial communities in diverse environments have led to the conclusion that planktonic growth rarely exists for microorganisms in nature [1]. Instead, bacteria preferentially form self-organized assemblages -- termed biofilms -- composed of surface-adherent cells embedded in a protective matrix comprised of extracellular polymeric substances (EPS) [1, 2]. Encased in this matrix of biopolymers, microbial communities develop physically diverse structures containing cell clusters, interstices, water channels [3], and large mushroom-shaped assemblies [4-9]. The transition from planktonic to biofilm mode of growth, and biofilm architecture are influenced by a range of local and macroscopic signals and stimuli, such as nutrient concentrations, intercellular communication, and environmental stresses [10-13].

Bacterial biofilms forming on damaged tissues [14-16] or on biomimetic devices [17-20], are a leading cause of chronic infections, since the cells within the biofilm are extremely resistant to antibiotics, and are adept at evading host immune responses. Interestingly, whereas biofilm-associated bacteria are more tolerant to antibiotics than their planktonic counterparts, it is only subpopulations within the biofilms -- termed persister cells -- that exhibit enhanced antibiotic **tolerance** [21-26]. This spatially nonuniform response to antibiotic treatment suggests that biofilms are comprised of structurally and functionally heterogeneous microcolonies that may differ from their surroundings with respect to metabolic activity, growth phase, and gene-expression patterns [27, 28]. For instance, in *P. aeruginosa* biofilms, it has been shown that dormant cells were more tolerant to tobramycin and silver ions. In addition, active cells had bigger cell size and higher intracellular density compared to dormant cells. It is possible that cells in these metabolically inactive microniches exhibit reduced antibiotic uptake rates. **In addition, drug tolerance in dormant cells has been attributed to lower cytoplasmic drug accumulation as a result of enhanced efflux activity [29].** Furthermore, these bacteria may be sheltered within a reaction-diffusion barrier presented by surrounding, faster-growing cells and EPS, thereby reducing local antibiotic penetration [30, 31].

Quorum sensing (QS) is a mechanism of intercellular communication used to collectively coordinate group behaviors based on population density [32-35]. This process relies on the production, release, and group-wise detection of signal molecules called autoinducers (e.g. acyl-homoserine lactones in Gram-negative bacteria) which rapidly diffuse in the liquid phase and across cell populations, and accumulate in the biofilm over time. Experimental work suggests that there is a positive correlation between QS and EPS production [36-39]. For instance, in *Pantoea stewartii* biofilms, approximately ten-fold increase in EPS production upon QS induction was observed [38]. **Cells exhibiting enhanced EPS production in the presence of autoinducer molecules are said to be up-regulated. QS-induced EPS production allows a biofilm to switch rapidly from a colonization mode to a protection mode** [40]. The EPS matrix confers structural integrity to the biofilm by providing mechanical strength, and reducing the extent of cell detachment [41, 42]. In addition, the effect of QS-regulated EPS production on

biofilm architecture has been shown to be a function of the growth stages during biofilm formation [43, 44].

The mechanisms of emergence of protected microcolonies in growing biofilms remain poorly understood. One possible explanation is nutrient limitation. When suspended in a solution of nutrients, microorganisms disrupt the uniform distribution of dissolved nutrients by locally depleting them and generating nutrient concentration gradients. The spatial distribution of accumulated biomass within the biofilm is, therefore, intimately interconnected with local nutrient concentration gradients. In addition, concentration gradients may also be set up for signaling molecules such as autoinducers resulting in spatially nonuniform production and distribution of EPS. Consequently, the biofilm may comprise of numerous microenvironments where local chemistries are distinctly different from the surroundings with respect to biomass density, nutritional availability, and concentrations of EPS and signaling molecules. Another possibility is that quorum-sensing signals allow the bacteria to trigger expression of protective genes, resulting in the formation of persister cells [45, 46].

A key challenge in modeling the structural development of a biofilm arises from the complex interaction between many processes. Current biofilm models can be broadly classified into two categories: continuum models [47, 48], and individual based models [49]. In continuum models, the biofilm is considered to be a continuous medium, with porosity, surface shape, and density as input parameters. In contrast, individual based models treat bacterial cells as individual units with their own states, thereby allowing for variability between individual behaviors with respect to their growth rates, nutrient uptake rates, local nutrient concentration, signaling molecule production, up-regulation and down-regulation states, and EPS production. The discrete, 3D nature of individual based models, combined with physical dynamics, allows for the calculation of concentration profiles of soluble entities, as well as the spatial distribution of biomass, and distribution in clusters. Consequently, chemical and structural heterogeneities within the biofilm emerge as a result of the actions and interactions of the cells with each other, and with the surrounding environment, rather than being a model input [49].

Several models have investigated quorum sensing in biofilms [50-52]. Most quorum sensing models focus on up-regulation, with only a few including the effect of quorum sensing on biofilm architecture, and growth dynamics [40, 53]. In many models, the cell density is assumed to be constant [54, 55], thereby neglecting biofilm expansion that results from the production of new cells, and shrinkage caused by cell death and detachment. Recently, attempts have been made to use deterministic continuum models of quorum sensing in biofilms [50]. Such models neglect the stochastic nature of the up- and down-regulation processes, and are unable to account for local heterogeneities in microbial subpopulations. In the past, mechanistic computational models have successfully described the autonomous formation of tertiary macrostructures in bacterial biofilms [56-58], including the effects of EPS on biofilm structure [59]. However, a systematic analysis of the local structural and chemical heterogeneities in the biofilm interior has not been performed. An analysis of the spatial heterogeneity in bacterial growth rates could shed light on mechanisms

of the emergence of dormant microcolonies containing cells that are potentially antibiotic-insensitive. Here, we present a prototype individual-based 3D computational cellular automata model to simulate biofilm growth, and quantify heterogeneity as a function of growth phase, space, and time. The goal is to answer the following questions: (i) can physical processes like nutrient starvation and localized cell death account for the formation of metabolically inactive microcolonies in biofilms, in the absence of genetic triggers? (ii) How does quorum sensing – and the associated EPS production – influence the structural heterogeneity of the biofilm? Specifically, we investigate the roles of (i) carbon source concentration, (ii) localized cell division, death, and dispersal, (iii) QS, and (iv) EPS production on the structural and chemical heterogeneity of mono-microbial biofilms. The model incorporates the following processes: nutrient diffusion, reaction, and convection; biomass growth kinetics, cell division, death, and dispersal; autoinducer production, and transport; and EPS production. The simulation represents a 400 h duration of biofilm growth, in which cells are tracked individually, allowing us to quantify spatiotemporal variations of heterogeneities of the biomass, EPS, nutrients, and signaling molecules.

Our results from causal modeling suggest that biofilms are comprised of at least three structurally distinct strata with respect to metabolic activity, growth phase, nutrient availability, and porosity: a high-biomass, low-heterogeneity section in the middle of the biofilm, sandwiched between two highly heterogeneous low-biomass regions on the top and the bottom. In QS-positive (QS^+) biofilms, an additional layer comprising of EPS, and devoid of cells, exists in close proximity to the substratum. The simulations show that nutrient limitation, in the absence of genetic triggers, can account for the formation of microenvironments containing dormant, low-activity cells surrounded by high-activity ones. Cell death occurs preferentially in the bottom section of the biofilm, leading to increase in heterogeneity in the biomass distribution in this region, and ultimately to sloughing. A clear understanding of heterogeneities at the local scale may be vital to solving the riddle of the resistance of biofilms to external stresses such as antibiotics.

Methods

Domain Geometry

The domain geometry used in this model is a 3D adaptation of the 2D domain described elsewhere [60]. Briefly, biofilm growth is simulated within the confines of a rectangular box. The bottom surface (square with side 120 µm) represents the stationary substratum upon which the biofilm develops. Periodic boundary conditions are applied in the horizontal directions, thereby eliminating edge effects, and ensuring continuity of biomass [58, 61]. A continuously replenished nutrient reservoir is placed at the top at a constant distance from the substratum. The interface between the nutrient reservoir and the biofilm domain is termed the diffusion boundary layer (DBL). It is assumed that the DBL has a constant thickness of 18 µm, and remains parallel to the substratum in the low-flow regime considered in this work. For the flow regime considered in this work, the nutrient concentration at a vertical distance of 18 µm from the highest cell in the biofilm was greater than 95% of the bulk nutrient concentration, even at time points corresponding to the highest cell numbers. It is worth noting that at high velocities, the diffusion boundary could follow the surface of the biofilm, and may not be necessarily stratified as is assumed here [62]. The space between the DBL and the substratum is discretized into cubical elements of volume 27 μm^3 each. During the simulation, each element may be occupied by one or more of the following entities: (i) bacterial cell, (ii) EPS, (iii) nutrient, and (iv) autoinducer. These entities are assumed to be capable of coexisting with each other in the same cubical element. The simulation represents a time march in which the occupancy status of each element is updated at every time step. At time $t = 0$, six cells, termed colonizers, are placed into random elements atop the substratum. Simultaneously, nutrient diffuses across the DBL. Cells consume nutrient, and subsequently grow and divide, resulting in the formation of a contiguous multicellular population. At the end of each time step, the nutrient reservoir is shifted vertically upwards such that a pre-determined distance from the topmost cell in the biofilm is always maintained. It is assumed here that the biofilm does not pose an obstacle to flow, and that it is subjected to a constant linear velocity gradient of 10 s^{-1} with zero velocity at the substratum, and maximum velocity at the highest point. **This latter is updated every time the height of the biofilm changes, so as to maintain a shear rate of 10 s^{-1}.**

It has been shown that giving up the conservation principles for fluid flow in the biofilm domain leads to increased deviations with respect to concentration fields and fluxes [63]. The magnitude of deviation is in some cases small (< 2 %, at slow bulk flow velocities of ~0.0001 m/s), and considerable in other (> 20 %, at fast bulk flow velocities of ~0.01 m/s). The results presented in this work correspond to the low bulk flow regime (maximum velocity of ~0.0006 m/s). Consequently, deviations in concentration fields and fluxes have been neglected. Such low fluid shear rates (10 to 50 s^{-1}), experienced within the intestine, and veins, have been shown to be effective in simulating S. aureus biofilm colonization and development [64, 65].

Using this domain geometry we were able to simulate biofilms containing up to 23368 ± 218 bacterial cells; recent individual-based models of biofilm formation and growth have shown that simulations involving up to 10,000 bacteria are sufficient to demonstrate that all steps of biofilm formation observed in experiments can be reproduced [66].

Each bacterial cell in the grid is modeled and tracked as an independent unit, with its own set of parameters (Table I) and behaviors. To simulate behavioral variability, parameter values for individual bacterial cells were obtained by random draws from a uniform distribution around the values listed in Table I while discarding all negative values, and those outside ±10% of the mean; these precautions are necessary with distributions ranging from $-\infty$ to $+\infty$ [67]. The resulting aggregate behavior of the biofilm is therefore emergent from the local interactions between the individual bacteria, and their surroundings, thereby allowing us to simulate the self-organized process of biofilm formation.

A detailed description of the different behaviors of the entities is presented below.

Nutrient Reaction and Transport

The spatial distribution of nutrient concentration within the biofilm influences biomass growth rate. In turn, bacterial behavior (growth, division, spreading, death, and detachment) affects nutrient concentration fields. The temporal and spatial distribution of nutrient concentration (C_N) is, therefore, intimately dependent on the local biomass concentration (C_B). $C_N = C_N(x, y, z, t)$ represents the nutrient concentration value at each element (x, y, z) of the spatial domain at time t. The nutrient uptake rate is described by the Herbert-Pirt model (Eq. 1) [68, 69].

$$r_N(C_N, C_B) = \left(\frac{\mu_{max}}{Y_{NB}} + m\right) C_B \left(\frac{C_N}{C_N + K_N}\right) \quad (1)$$

where μ_{max}, Y_{NB}, and m represent the maximum specific growth rate, yield coefficient, and maintenance coefficient of the bacteria, respectively, and K_N is the half-saturation coefficient.

The nutrient concentration within each element of the domain changes because of consumption, diffusion, and convection, and is given by

(2)

$$\frac{\partial C_N}{\partial t} = -r_N(C_N, C_B) + D_N \sum_{i=1}^{3} \frac{\partial^2 C_N}{\partial x_i^2} - \nabla \cdot (v C_N)$$

Here, D_N is the nutrient diffusivity, and v is the local fluid velocity. Diffusion coefficients within bulk flow (region with no biomass) and the biofilm domain (region with biomass) are assumed to be identical, i.e. solutes diffuse through liquid-filled and biomass-filled regions at the same rates. The 3D reaction–diffusion-convection equation is solved numerically with the following boundary conditions:

a) A Dirichlet boundary condition is imposed at the DBL, i.e., the nutrient concentration remains constant at the interface between boundary layer and bulk liquid.
b) Neumann boundary condition is imposed at the substratum, where the nutrient flux is zero.
c) Periodic boundary conditions are applied at the lateral boundaries.

A portion of the consumed nutrient is utilized by the bacterium towards endogenous metabolism. The leftover nutrient is assumed to be converted to biomass with an efficiency called the yield coefficient, Y_{NB} [60]. The net accumulation of biomass is, therefore, given by:

$$\frac{\partial C_B}{\partial t} = Y_{NB}[r_N(C_N, C_B) - mC_B] \quad (3)$$

Real biomass growth is governed by the specific growth rate, μ_{max}, and decay of biomass is included by incorporating the maintenance coefficient, m, and yield coefficient, Y_{NB}. This allows for negative net biomass growth under low nutrient conditions.

Cell Division, Death, and Detachment

Cell division

When the biomass of a bacterium reaches twice its native value it divides into two daughter cells. Whereas one daughter cell continues to remain in the same element as the dividing mother cell, the other is pushed into a bacterium-free element in the immediate neighborhood. The immediate neighborhood, termed the Moore neighborhood, comprises of 26 cubical elements surrounding the central element. If multiple bacterium-free elements are available for occupation, one is chosen at random [69]. On the other hand, if all elements in the Moore neighborhood are occupied by bacteria, an unoccupied element is identified at the nearest Chebyshev distance from the location of the mother cell. The occupancy statuses of elements is checked at successively larger Chebyshev distances (starting with a Chebyshev distance of 2, and moving outward, layer by layer), until an empty element is found. Each of the bacterial cells that lie between the mother cell and the closest bacterium-free element is then shifted by one grid element – away from the mother cell, and towards the empty element – creating a bacterium-free element in the Moore neighborhood of the mother cell. This newly created bacterium-free element is then occupied by

the daughter cell, thereby ensuring that the daughter cell is always placed immediately next to the dividing bacterium.

Cell death

Cell death is assumed to occur via one of two mechanisms: (i) limited nutrient uptake [70], or (ii) starvation caused by prolonged stay in the stationary phase [71, 72]. Nutrient uptake is quantified by the ratio (R) of the rate of biomass formation $(Y_{NB}r_N(C_N, C_B))$ to that of endogenous metabolism $(Y_{NB}mC_B)$ (Eq. 3). Cell death by limited nutrient uptake is assumed to occur when R falls below a certain threshold (R_{min}) [60]. Along similar lines, if R falls below 1, the cell exhibits zero or negative net growth, and is said to have entered the stationary phase. Cell death is assumed to occur if the cell remains in this growth-arrested phase for a preset number of hours (t_{SP}). This is consistent with observations where bacteria in the stationary phase gradually lose their ability to reproduce, and exhibit signs of senescence and eventually loss of viability by accumulating oxidatively damaged proteins [71, 72]. The spatial locations of cell death events are recorded at each time step for further analysis. Subsequently, dead cells are discarded from the simulation domain, and are no longer tracked. Experimental work involving biofilms grown in flow cells has shown that hollow cell clusters are formed, and that lysed cells are apparent in the internal strata [70]. Furthermore, it has been suggested that approximately 50 cells must die in order to support one cell division [73]. Extensive modeling work in the past where lysed cells contributed nutrients to the neighboring cells found no significant difference in the results [60]. Therefore, the contribution of nutrients from lysed cells has been omitted here.

Cell detachment

Cell detachment in bacterial biofilms is a complex process influenced by a host of external and internal factors such as fluid shear forces [74], internal stresses [75], chemical gradients [76], erosion [74], and nutrient starvation [70]. Here, we implement a simplified geometrical model wherein cell detachment is governed by (i) localized cell death resulting from nutrient limitation, and (ii) EPS formed as a consequence of quorum sensing. Cell detachment is determined by evaluating the connectivity of cells to the substratum. Within the biofilm, bacteria connect to the substratum either directly, or indirectly through a group of live bacteria in which at least one bacterium is directly bound to the substratum [77]. In addition to live bacteria, in QS^+ biofilms, cells can also continue to remain connected to the substratum via EPS. At the end of each time step, detachment events are recorded, and detached cells are removed from the domain.

Quorum Sensing

In QS^+ biofilms, bacterial cells are modeled as being in either the up-regulated, or the down-regulated state. Cells switch between these states at rates dependent on the local autoinducer concentration (C_A). The transition rate from the down-regulated to up-regulated state is given by

(4)

$$TR^{+} = \alpha \frac{C_A}{1 + \gamma C_A}$$

Along similar lines, the transition rate between the up-regulated to down-regulated states is given by [51]

$$TR^{-} = \beta \frac{1}{1 + \gamma C_A} \tag{5}$$

where α and β are the spontaneous up- and down-regulation rates, and γ is the transition constant. The probabilities of switching from one state to another within a time interval of Δt are then given by

$$\begin{aligned} P_u &= (TR^{+})\Delta t \\ P_d &= (TR^{-})\Delta t \end{aligned} \tag{6}$$

where P_u is the probability of up-regulation, and P_d is the probability of down-regulation.

Autoinducer Production and Transport

Up-regulated and down-regulated cells are assumed to secrete autoinducer molecules at constant rates of $r_{A,u}$ and $r_{A,d}$, respectively.

$$r_A = \begin{cases} r_{A,u} \\ r_{A,d} \end{cases} \tag{7}$$

where $r_{A,u} > r_{A,d}$(Table I). The secreted autoinducer is treated as a dissolved entity that is transported via diffusion and convection. The time evolution of the autoinducer concentration within the biofilm is given by

$$\frac{\partial C_A}{\partial t} = D_A \sum_{i=1}^{3} \frac{\partial^2 C_A}{\partial x_i^{\,2}} + \frac{r_A}{\Delta V} - \nabla \cdot (v C_A) \tag{8}$$

where D_A is the autoinducer diffusivity, and ΔV is the element volume. Eq. 8 is subject to the Dirichlet boundary condition at the DBL ($C_{A,DBL} = 0$), and the no-flux condition at the substratum.

EPS Production

EPS is treated as a discrete entity and is tracked individually in a manner similar to that of a bacterial cell. EPS and bacteria are assumed to be capable of coexisting in the same element. Furthermore, quantities of EPS and bacterial biomass that can be accommodated in a single element are assumed to be independent of each other. Consequently, new bacterial cells embed themselves into EPS, instead of pushing it aside. This is consistent with previous experimental work showing the accumulation of extracellular polysaccharides such as β-glucan found intercalating between micro colonies of *Streptococcus mutans* [78]. Bacterial growth and EPS

production are assumed to occur concurrently from nutrient that is leftover after maintenance has been accounted for. It is assumed that EPS is produced only by upregulated cells, at a rate given by

$$\frac{\partial C_E}{\partial t} = Y_{NE}[r_N(C_N, C_B) - mC_B]$$

where, Y_{NE} is the yield coefficient for EPS, i.e. the efficiency with which nutrient that has not been consumed for endogenous metabolism is converted to EPS. EPS division is handled similar to cell division described above, wherein daughter "EPS cells" are placed into the nearest element that does not contain EPS.

In QS^+ biofilms, upregulated cells secrete EPS and autoinducer molecules at an enhanced rate, compared to their downregulated counterparts. In a feedback-like mechanism, enhanced production of autoinducer by upregulated cells results in the upregulation of an increasing number of cells in the neighborhood.

Heterogeneity

Biofilm heterogeneity, h, was defined as the extent of nonuniform distribution of a selected component, and was quantified as the coefficient of variation with respect to the total accumulated biomass, and nutrient, EPS, and autoinducer concentrations.

$$h = \frac{\sigma}{\mu} \tag{10}$$

where, σ is the standard deviation, and μ is the mean of the quantity whose heterogeneity is being evaluated. Thus, h measures the extent of variability with respect to the mean of the population. Two separate calculations were performed for each component: (i) an overall heterogeneity to track the variability throughout the entire domain, and (ii) a grid-layer-wise evaluation to delineate the spatial variation of heterogeneity. For the former, σ and μ were computed over the entire biofilm domain, whereas for the latter calculations were performed over individual grid layers.

Model Simulation and Numerical Scheme

The state of the simulation domain is updated at discrete time steps**.** Previous work analyzing the kinetics of the switching process from the vegetative state to the competent (EPS producing) state of *Bacillus subtilis* has shown that the duration of the switching period was 1.4 ± 0.3 h [79]. In addition, analysis of *Bacillus subtilis* at the interface between the culture medium and air indicates that bacteria switch from the motile to the matrix-producing phenotype (downregulated to upregulated) between 10 min to 1h [66]. **Consequently, here we use a multiscale integration approach with two distinct time scales are used:** (i) Cellular processes (biomass growth (Eq. 3), EPS production (Eq. 9), switching between up- and down-regulated states (Eq. 6), division, death, and detachment) are monitored every 1 h, and (ii) Within this "outer" time loop, concentrations of dissolved entities (nutrient (Eq. 2), and autoinducer (Eq. 8)) are tracked by solving the diffusion-convection equations at a finer time resolution of $1x10^{-6}$ h. Numerical solutions to the

diffusion-convection equations are obtained using a second-order Forward-Time Central-Space scheme. Periodic boundary conditions are applied in the horizontal directions, and the Dirichlet boundary condition is imposed in the vertical direction. The Java programming language is used since it provides a convenient object-oriented framework that is well-suited for the individual based model described here.

The parameter values used in the model are summarized in Table I.

Table I. Model parameters

Parameter	Description	Value	Unit	Reference
	Element length	3		
	Thickness of the DBL	18		[60]
	Number of elements in the irection	40		
	Initial number of bacterial cells	6		
	Maintenance coefficient	0.036	h	[60]
	Maximum specific growth rate of bacterial population	0.3125	h	[60]
	Yield coefficient for biomass	0.45		[60]
	Time in the stationary phase at which cell death occurs	24	h	[60]
	Ratio of the rate of nutrient consumption to that of endogenous metabolism below which cell death occurs	0.15		[60]
	Threshold biomass at which cell division occurs	**2 x 10^{-12}**		
	Diffusion coefficient of nutrient	0.84 x 10^{-6}		[60]
	Monod saturation constant	2.55		[60]
	Bulk nutrient concentration	1, 4, 8		
	Yield coefficient for EPS	0.27		
	Threshold concentration at which EPS division occurs	**33000**		
	Diffusion coefficient of autoinducer	1 x 10^{-6}		
	Autoinducer production rate by up-regulated cells	73800		[51]
	Autoinducer production rate by down-regulated cells	498		[51]
	Spontaneous up-regulation rate	7.89 x 10^{-17}		[51, 80]
	Spontaneous down-regulation rate	0.975	h	[51, 80]

	Transition constant	7.96×10^{-17}		[51, 80]

1

Results and Discussion

Biofilm growth dynamics: Influence of nutrient concentration

As a first step, we simulated biofilm growth dynamics for a QS-negative (QS^-) strain that does not produce autoinducer or EPS. At time $t = 0$, six colonizers were placed at random locations on the substratum. Nutrient diffuses into the domain across the DBL, and is subsequently consumed by bacterial cells, thereby causing their biomass to increase. This, in turn leads to cell growth, division, and expansion of the biofilm. Fig. 1 shows a representative time evolution of a QS^- biofilm associated with a bulk nutrient concentration of 4 gm^{-3}, illustrating the formation of a distinct 3D macrostructure as the biofilm matures, and the various growth stages including: (i) colonization, (ii) early exponential phase, (iii) late exponential phase, (iv) maturation, (v) sloughing, and (vi) regrowth.

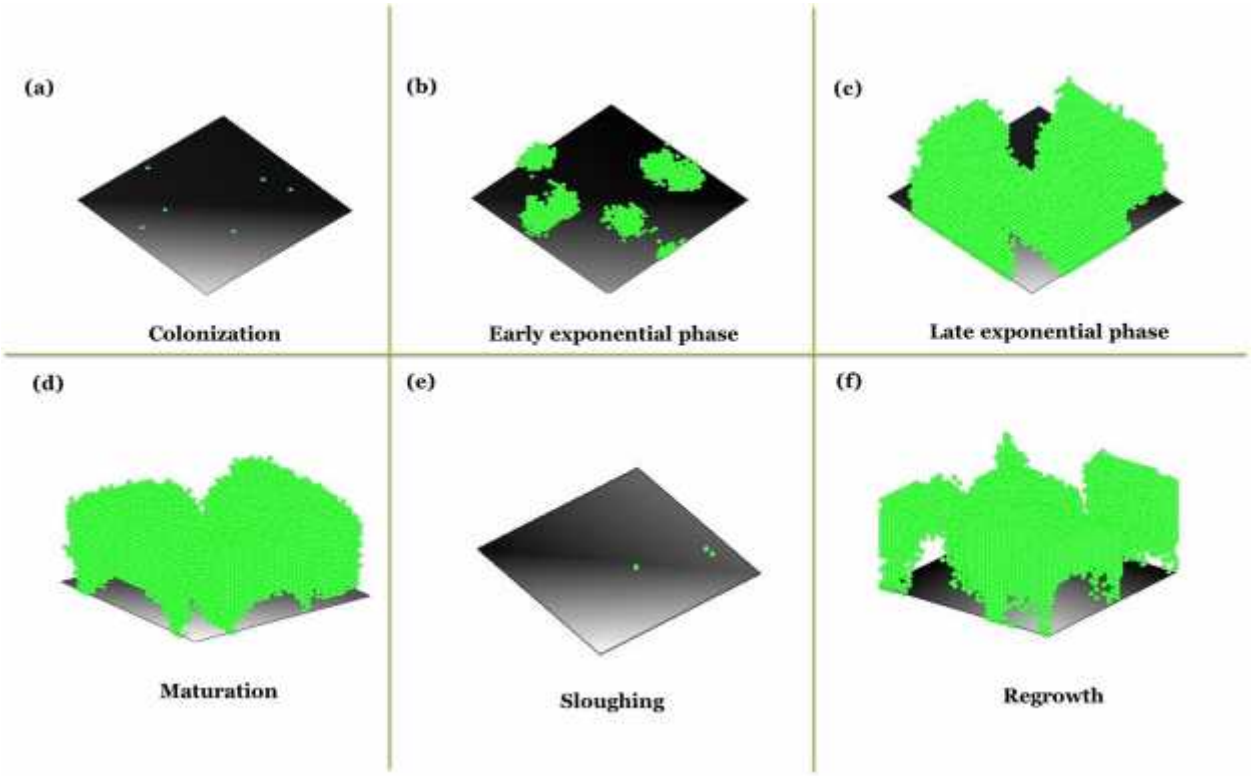

Fig. 1. Representative 3D renderings of the time evolution of a QS^- biofilm for $C_{N,bulk}$ = 4 gm^{-3}, illustrating different phases of growth at 0 h (a), 30 h (b), 60 h (c), 110 h (d), 120 h (e), and 330 h (f).

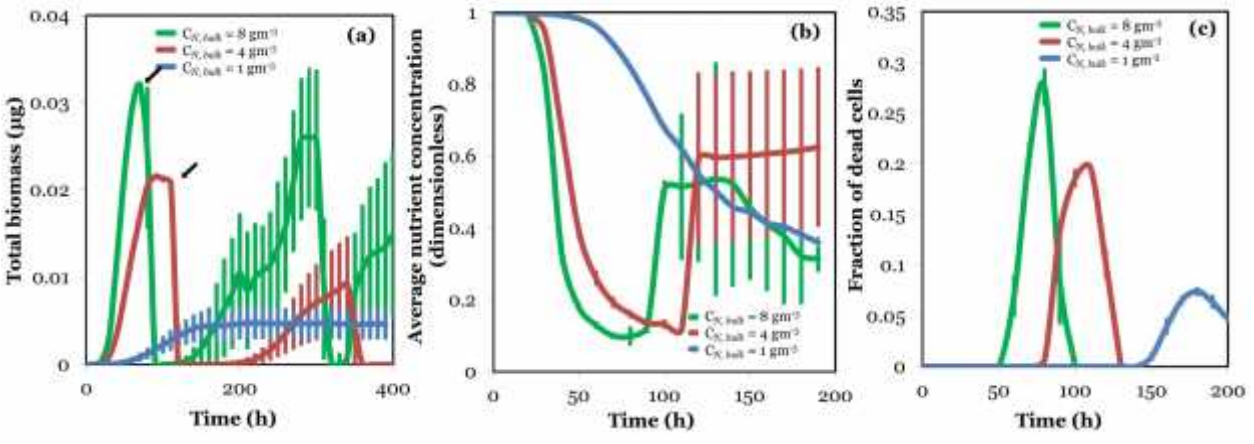

Fig. 2. **Growth dynamics for QS$^-$ biofilms**. Comparison of the development of total biomass (a), average nutrient concentration (b), and fraction of dead cells (c) for $C_{N,bulk}$ = 8 gm^{-3} (green), 4 gm^{-3} (red), and 1 gm^{-3} (blue). The arrows in panel (a) mark the end of the stationary phase and the initiation of sloughing for $C_{N,bulk}$ = 8 gm^{-3} and $C_{N,bulk}$ = 4 gm^{-3}. Data represent mean ± standard error of mean (SEM) of four separate simulations.

To delineate the influence of nutrient availability on biofilm growth, we tracked the total accumulated biomass and average nutrient concentrations within the biofilm for varying bulk nutrient concentrations (1, 4, and 8 gm^{-3}), in the absence of QS (Figs. 2a, 2b). In close agreement with experimental evidence [81, 82], the model was able to simulate four distinct growth phases: exponential growth, stationary phase, sloughing, and regrowth. Biofilm growth rates and peak cell numbers in the exponential phase increased with increasing bulk nutrient concentrations (Fig. 2a, Table II). In close agreement with experimental observations [83], sloughing in the faster growing biofilms ($C_{N,bulk}$ = 8 gm^{-3}) occurred earlier (~80 h) compared to the slower growing ones ($C_{N,bulk}$ = 4 gm^{-3}; ~110 h). Re-growth of the biofilm occurred post-sloughing. There is considerable variability between results across simulation runs in this phase, due to the high sensitivity to the conditions post-sloughing – i.e., the number of cells that survive detachment (Fig. 2a). Whereas under moderate ($C_{N,bulk}$ = 4 gm^{-3}) and excess ($C_{N,bulk}$ = 8 gm^{-3}) nutrient supply conditions, the average nutrient concentration within the biofilm dropped rapidly in the exponential growth phase, there was a gradual decrease when the nutrient supply was low ($C_{N,bulk}$ = 1 gm^{-3}) (Fig. 2b). Post-sloughing, due to the marked decrease in the total accumulated biomass, the average nutrient concentration increased rapidly (Fig. 2b).

The marked decline observed in the total biomass content of the biofilm at the end of the stationary phase could be a consequence of either (i) annihilation of the bacterial population in its entirety, or (ii) live cells detaching from the substratum (sloughing). To investigate which of these two possibilities was predominantly responsible for the drop in biomass, we tracked the fraction of dead cells with time. As shown in Fig. 2c, peak cell death occurred just prior to sloughing (for $C_{N,bulk}$ = 8 gm^{-3} ~30% of the cells die at ~80 h; for $C_{N,bulk}$ = 4 gm^{-3} ~20% of the cells die at ~110 h).

Since the fraction of dead cells was much less than 1 under all conditions tested, we conclude that the drastic reduction in the biomass is a consequence of live cells losing contact with the substratum, because of cell death occurring in the lower layers of the biofilm.

The biofilm associated with the bulk nutrient concentration of 1 gm^{-3} exhibited a prolonged stationary phase in which both the total biomass (Fig. 2a) and the fraction of dead cells (Fig. 2c) remained virtually constant, indicating that a balance was established between the rates of biomass formation and depletion. Sloughing did not occur under these conditions. This could be the consequence of the fact that under these nutrient-depleted conditions cells die at a slow rate, which ensures the presence of enough number of cells at the bottom of the biofilm to keep it attached to the substratum at all times.

Biofilm growth dynamics: Influence of QS

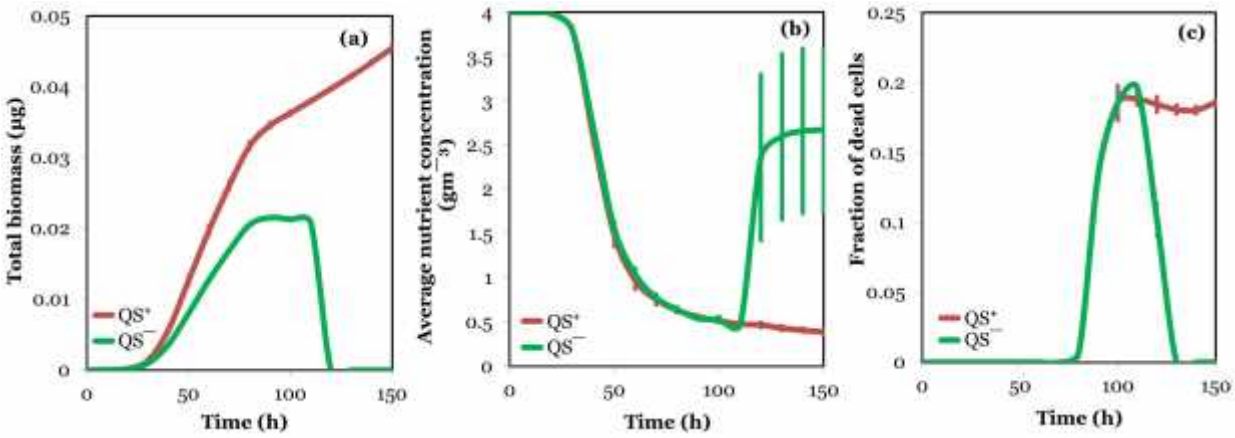

Fig. 3. **Influence of QS on biofilm growth dynamics**. Comparison of total accumulated biomass (a), average nutrient concentration (b), and fraction of dead cells (c) for QS^+ (red) and QS^- (green) biofilms for $C_{N,bulk}$ = 4 gm^{-3}. The total biomass for the QS^+ biofilm includes mass of the EPS produced by upregulated cells. Data represent mean ± SEM of four separate simulations.

QS had minimal impact on the bacterial growth rates during the exponential growth phase (Table II). The total biomass (bacteria + EPS) was higher than that for the EPS-devoid QS^- biofilm in both the exponential and stationary growth phases. In stark contrast to the QS^- biofilm, the QS^+ biofilm exhibited a prolonged stationary phase; no sloughing occurred even for the bulk nutrient concentrations of 4 gm^{-3} (Fig. 3a) and 8 gm^{-3} (data not shown), because of the presence of EPS which prevents live cells from detaching. QS did not alter the growth dynamics of the biofilm under low nutrient supply conditions ($C_{N,bulk}$ = 1 gm^{-3}), even in the stationary phase (data not shown). Taken together with the observation that QS^- biofilms were resistant to sloughing under these conditions (Fig. 2a), this result indicates that EPS plays a limited role in stabilizing the biofilm structure under low nutrient conditions. The average nutrient concentration decreased monotonically with time in the exponential growth phase, and then remained virtually constant (Fig. 3b). For $C_{N,bulk}$ = 4 gm^{-3}, first instances of cell death were observed at ~80 h; peak cell death occurred at 100 h, and then remained virtually constant (Fig. 3c).

Table II. Biomass growth and EPS production rates.

$C_{N,bulk}$ (gm^{-3})	Growth rate of bacterial biomass ($gm^{-3}\ h^{-1}$)*		Production rate of EPS ($gm^{-3}h^{-1}$)*
	QS^-	QS^+	
1	48.5 ± 6.3	54.7 ± 19.1	29.1 ± 8.7
4	256.8 ± 29.5	295.7 ± 19.3	191.3 ± 21.9
8	492.1 ± 32.5	519.5 ± 15.1	329.6 ± 23.5

** Rates of bacterial biomass growth and EPS production were calculated as the net increase in bacterial biomass or EPS per unit time for the duration of the exponential growth phase (60 h for $C_{N,bulk}$ = 8 gm^{-3}, 80 h for $C_{N,bulk}$ = 4 gm^{-3}, and 170 h $C_{N,bulk}$ = 1 gm^{-3}).*

QS-induced upregulation of cells and EPS Production

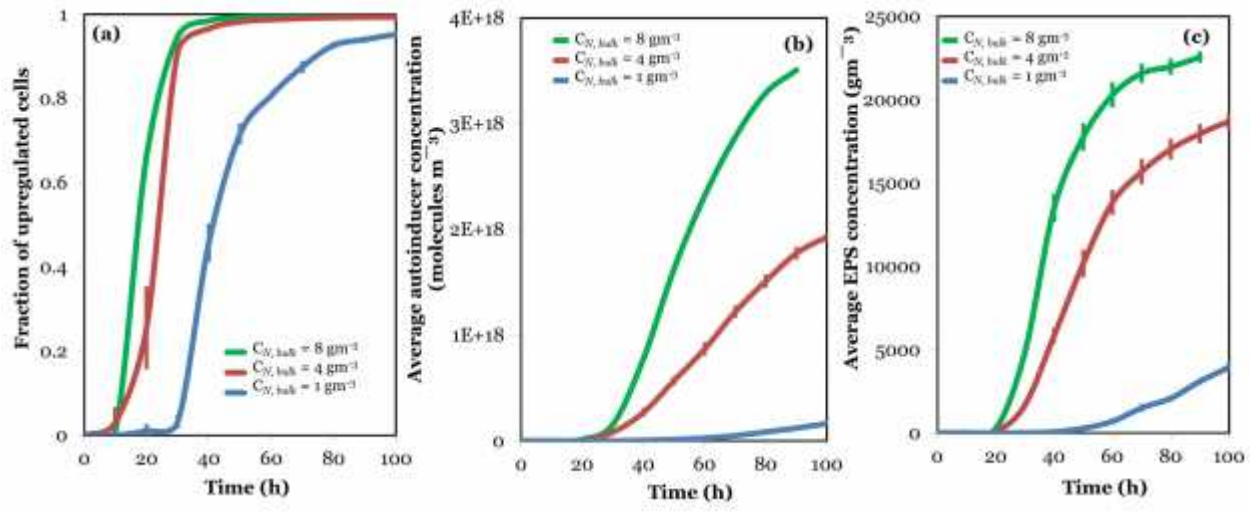

Fig. 4. The fraction of upregulated cells (a), and average autoinducer (b) and EPS (c) concentrations for $C_{N,bulk}$ = 8 gm^{-3} (green), 4 gm^{-3} (red), and 1 gm^{-3} (blue). Data represent mean ± SEM of four separate simulations.

Cells in the QS^+ biofilm produced and locally released autoinducer molecules which spread throughout the biofilm via diffusion and convection. After the autoinducer concentration reached a threshold value, nearby bacterial cells upregulated resulting in the enhanced production of the autoinducer as well as that of EPS. The fraction of upregulated cells increased during the exponential growth phase until virtually the entire biofilm rapidly switched from low to high QS activity (Fig. 4a). This switch was delayed under low nutrient supply conditions ($C_{N,bulk}$ = 1 gm^{-3}). The average autoinducer concentration increased monotonically with time for all three bulk nutrient concentrations (Fig. 4b). Analogous to the variation of total accumulated biomass, the average EPS concentration in the biofilm also increased rapidly with time in the exponential growth phase, before plateauing in the stationary phase (Fig. 4c). The rate of EPS production during the exponential growth phase was highest for the bulk nutrient concentration of 8 gm^{-3}, and

decreased for the lower bulk nutrient concentrations (Table II).

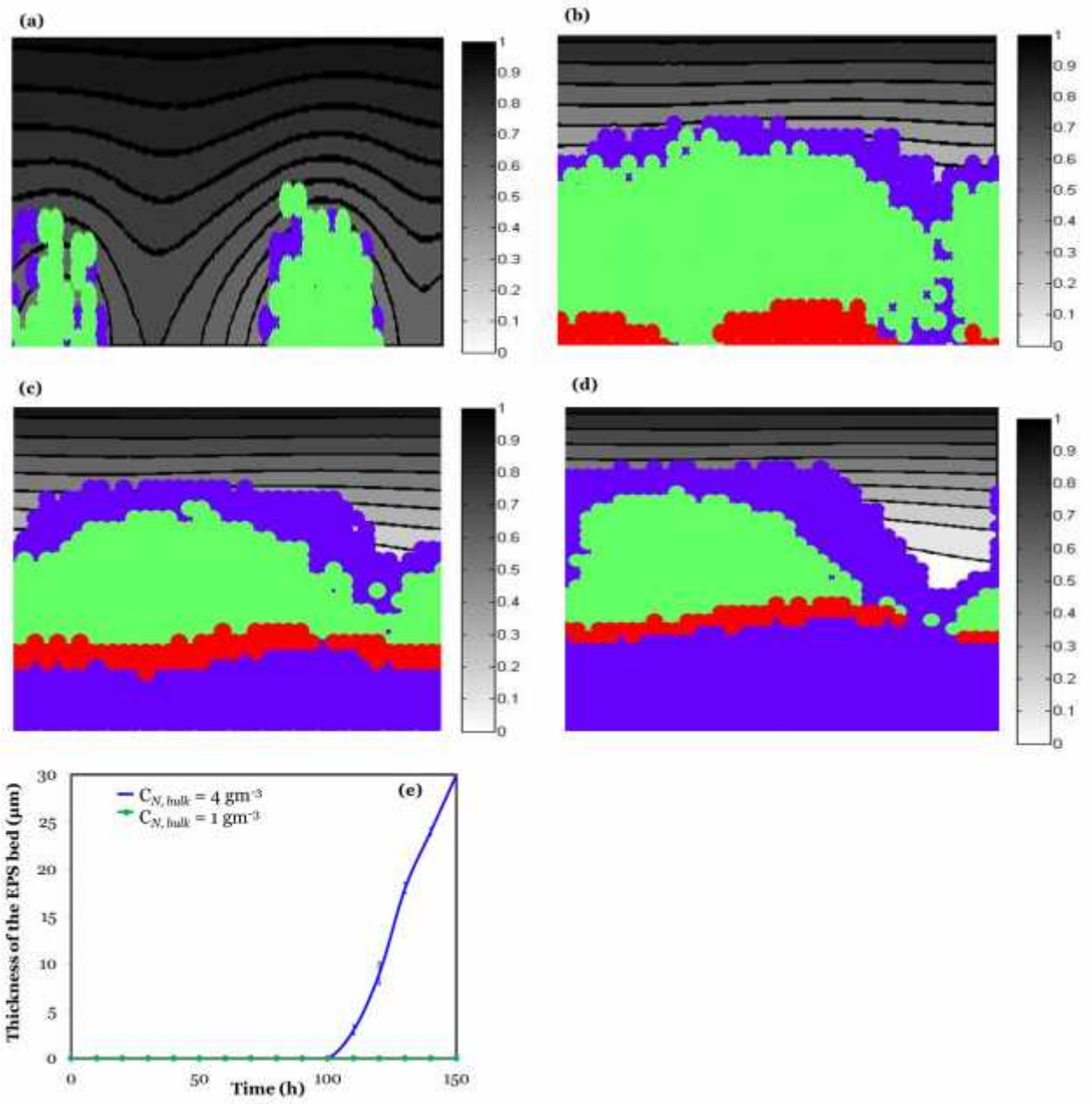

Fig. 5. **Distribution of EPS**. Visualization of 2D cross-sections showing live cells (green), locations of cell death (red), and EPS without cells (purple) of the QS^+ biofilm for $C_{N,bulk}$ = 4 gm^{-3} at 40 h (a), 90 h (b), 120 h (c), 150 h (d). It is to be noted that the green and red elements may also contain EPS. The isolines show the nutrient concentration distribution. The thickness of the cell-devoid EPS bed for $C_{N,bulk}$ = 4 gm^{-3} (blue) and $C_{N,bulk}$ = 1 gm^{-3} (green) is shown in panel (e).

For $C_{N,bulk}$ = 4 gm^{-3}, upon initiation of cell death (~80 h) on the bottom layers, a bed of EPS -- devoid of cells -- developed adjacent to the substratum upon which the rest of the biofilm grew (Figs. 5b, c, and d). The height of the EPS bed increased with time (Fig. 5e). These results clearly indicate that production of EPS by upregulated cells -- and its subsequent accumulation in the lower regions of the biofilm -- plays a key role in stabilizing the biofilm structure by reducing detachment events. Formation of the EPS bed was not observed for $C_{N,bulk}$ = 1 gm^{-3} (Fig. 5e), validating the idea that under depleted nutrient conditions, bacterial cells at the bottom hold the biofilm together, and that EPS plays a limited role.

Formation of metabolically dormant cellular micro-compartments

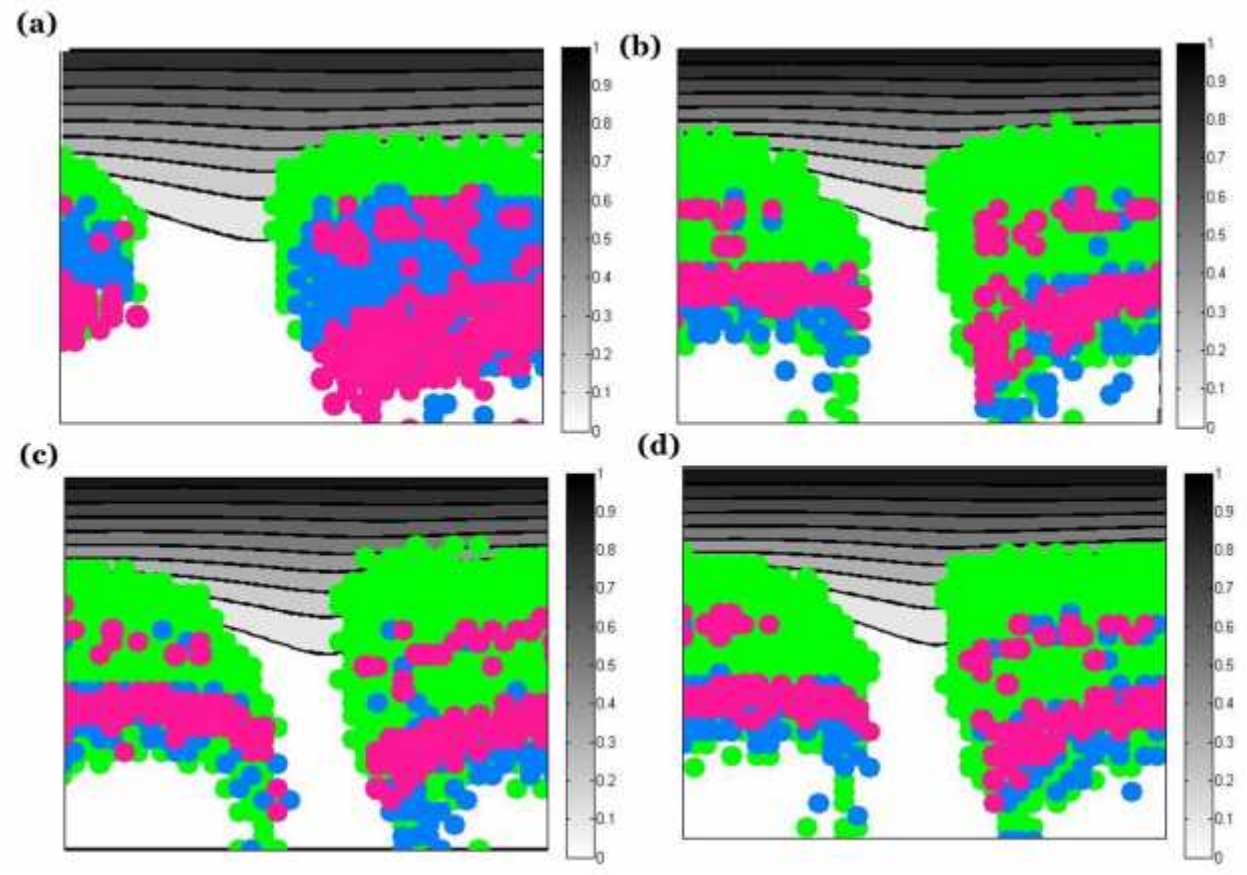

Fig. 6. Illustrative cross-sections showing metabolically inactive cellular micro-compartments in QS^- biofilms for $C_{N,bulk}$ = 8 gm^{-3} at 70 h; cells are categorized into three distinct subpopulations with high (green; greater than 3600 $gm^{-3}h^{-1}$), intermediate (blue; 425-3600 $gm^{-3}h^{-1}$), and low (pink; less than 425 $gm^{-3}h^{-1}$) growth rates.

Next, we categorized cells into three groups based on their growth rates as follows: dormant cells (growth rate less than 425 $gm^{-3}h^{-1}$), and those exhibiting high (greater than 3600 $gm^{-3}h^{-1}$), and intermediate (425-3600 $gm^{-3}h^{-1}$) growth rates. Fig. 6 shows representative cross-sections of the mature biofilm associated with the bulk nutrient concentration of 8 gm^{-3}, illustrating the formation of microcolonies in the lower and intermediate layers of the biofilm structure. Low-activity cells (red) were encased within cell clusters of high activity (green). Similar micro-compartments were observed for QS^+ biofilms (data not shown). In our model, the cellular growth rates are

influenced by two variables: C_N, and C_B (eq. 3). Based on these factors, we propose two possible explanations for the presence of dormant cellular microcolonies in the biofilm: (i) horizontal nutrient concentration gradients may be set up, resulting in increased nutrient concentrations in the lower layers, and hence higher cellular growth rates; and (ii) cells in the red regions may have lower biomass (possibly being newly divided) compared to cells in the green regions underneath, once again resulting in lower nutrient consumption rates, and hence lower growth rates.

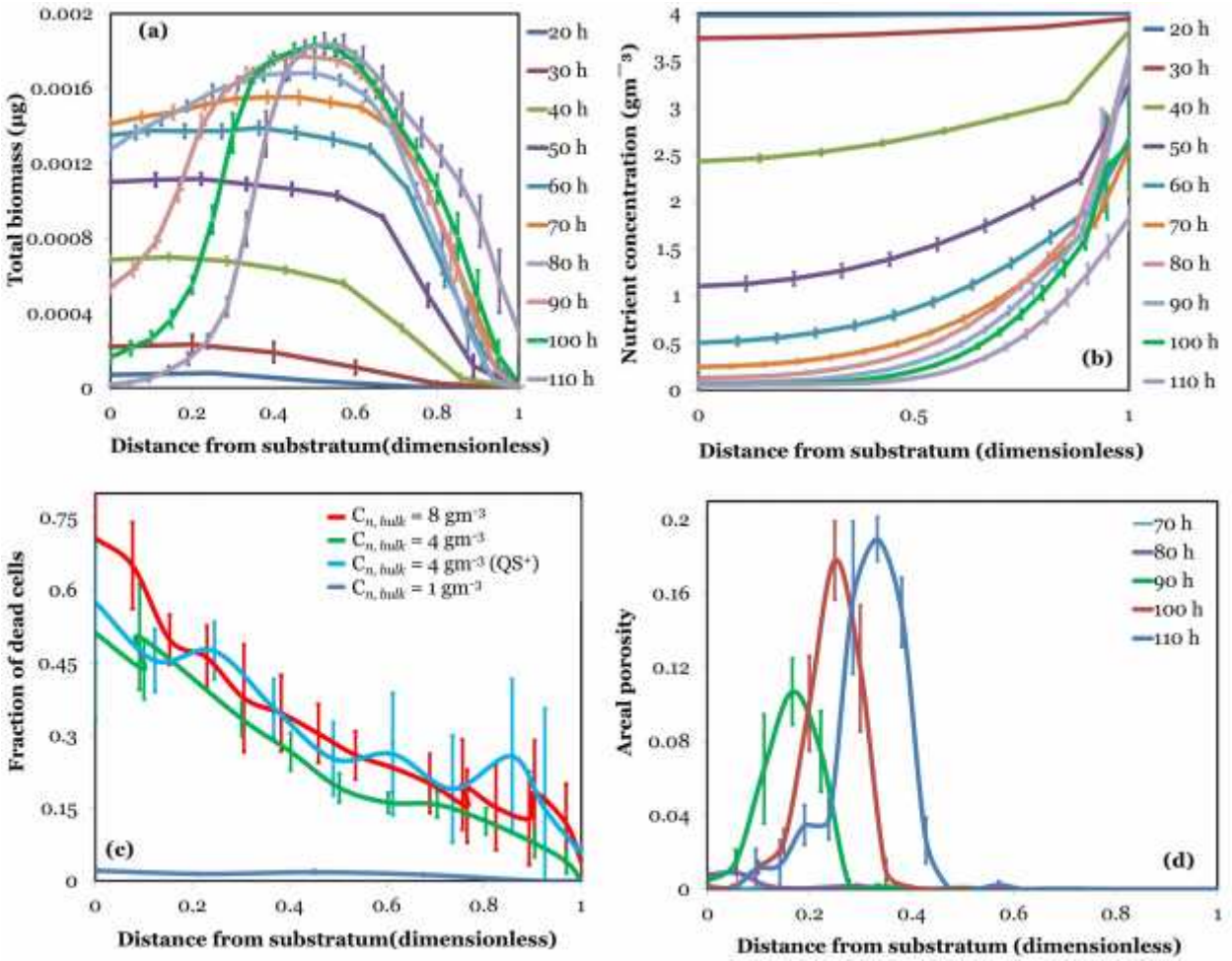

Fig. 7. Distributions of biomass (a), nutrient concentration (b), fraction of dead cells (c), and areal porosity (d) at varying distances from the substratum for $C_{N,bulk}$ = 4 gm^{-3} for growth times of 20-110 h. The fractions of dead cells in (c) are reported at the time of sloughing for the respective bulk nutrient concentrations. Data represent mean ± SEM of four separate simulations.

To investigate the spatial variation of heterogeneity, we determined the distribution of biomass and nutrient concentrations at varying distances from the substratum for the bulk nutrient concentration of 4 gm^{-3}. In the early and late exponential growth phases (up to 70 h), the biofilm was homogeneous in the lower and intermediate layers with uniform biomass distribution. The distribution in the upper layers was non-uniform, with biomass decreasing rapidly with increasing

distance from the substratum (Fig. 7a). The heterogeneity at the top layers is a consequence of the fact that during cell division new daughter cells are randomly placed in the closest neighboring locations.

The biomass distribution underwent a dramatic change in the late exponential phase (80-110 h) with a high proportion of the biomass concentrated in the intermediate layers (25-40 μm from the substratum) (Fig. 7a). In contrast, the nutrient concentration decreased monotonically with decreasing distance from the substratum (Fig. 7b), indicating that a large portion of the nutrient is consumed at the surface, and in the intermediate layers leading to nutrition-depleted niches in the depths. However, it should be noted that under these conditions nutrient concentration levels in the lower layers was high enough to not cause cell death (Fig. 2c).

The value of the maximal biomass and the height at which it occurred increased with time (Fig. 7a). For instance, at 60 h maximal biomass is observed at a height of 12 μm (0.0014 μg). On the other hand, at 110 h maximal biomass is observed at a height of 33 μm (0.0018 μg). Biomass in the layers in close proximity to the substratum declined rapidly due to cell death occurring in this region of the biofilm (Fig. 7c). This can be explained by the fact that in the stationary growth phase the nutrient concentrations reduced to very low levels ($<0.2 \pm 0.06$ gm^{-3}) within a distance of 24 μm from the substratum (Fig 7b). This, in turn, is a consequence of the fact that cells in the topmost and intermediate layers of the biofilm consume nutrient, allowing less of it to penetrate to the depths of the biofilm.

Immediately prior to sloughing, maximal cell death was observed in the lower layers of the biofilm for bulk nutrient concentrations of 4 and 8 gm^{-3} (Fig. 7c). Approximately three-fourths of the cells on the lowest layer died for $C_{N,bulk} = 8$ gm^{-3}, whereas a little over half the cells on the lowest layer died for $C_{N,bulk} = 4$ gm^{-3}. On the other hand, for the lowest bulk nutrient concentration of 1 gm^{-3}, the distribution of dead cells remained virtually constant across all layers of the biofilm (Fig. 7c). Sloughing did not occur under these conditions (Fig. 2a).

Interestingly, for the highest bulk nutrient concentration (8 gm^{-3}), cell death happened due to starvation (low nutrient consumption-to-maintenance ratio) whereas for the intermediate and low bulk nutrient concentrations (1, 4 gm^{-3}), cell death occurred due to cells being in the stationary phase for the prescribed limit (24 h). Along these lines, nutrient availability -- and hence the nutrient consumption rate -- in the lower layers was less for the higher bulk nutrient concentration of 8 gm^{-3} compared to that for $C_{N,bulk} = 4$ gm^{-3} and $C_{N,bulk} = 1$ gm^{-3}. For instance, the average nutrient concentrations at the dimensionless biofilm height of 0.5 increased with decreasing bulk nutrient concentrations (0.08 ± 0.007 gm^{-3}, 0.26 ± 0.03 gm^{-3}, and 0.95 ± 0.01 gm^{-3} for bulk nutrient concentrations of 8 gm^{-3}, 4 gm^{-3}, and 1 gm^{-3}, respectively). Consequently, amongst the three bulk nutrient concentrations studied, the nutrient consumption rates near the substratum were the lowest for $C_{N,bulk} = 8$ gm^{-3} compared to those for $C_{N,bulk} = 1, 4$ gm^{-3}. A similar behavior was observed for QS^+ biofilms (Fig. 7c).

Thus, there was a negative correlation between the bulk nutrient concentration and nutrient availability in the lower regions of the biofilm, with nutrient availability being the lowest for the highest bulk nutrient concentration of 8 gm^{-3}, and the highest for the bulk nutrient concentration of

1 gm^{-3}. This effect became more pronounced towards the end of the exponential growth phase, as the biofilm approached the stationary phase. This can be explained by the fact that because of the high growth rate, the number of cells/total biomass in the intermediate regions is highest for $C_{N,bulk}$ = 8 gm^{-3} . This, in turn, causes the nutrient consumption rates to be high, consequently reducing the availability of nutrients in the lower regions.

The areal porosity was minimal in the exponential growth phase (up to 80 h) (Fig. 7d). Subsequently, in the stationary phase, areal porosity increased with time. This is a consequence of an upsurge in cell death events in the stationary phase, thereby creating cell-devoid pockets in the interior of the biofilm. Maximal areal porosity was observed in the intermediate layers, and decreased for layers closer to the substratum. This indicates that although the biomass density near the substratum is low, the biofilm is more compact in this region. Prior to sloughing, the biomass and nutrient distributions were found to be similar for the QS$^+$ biofilms (data not shown).

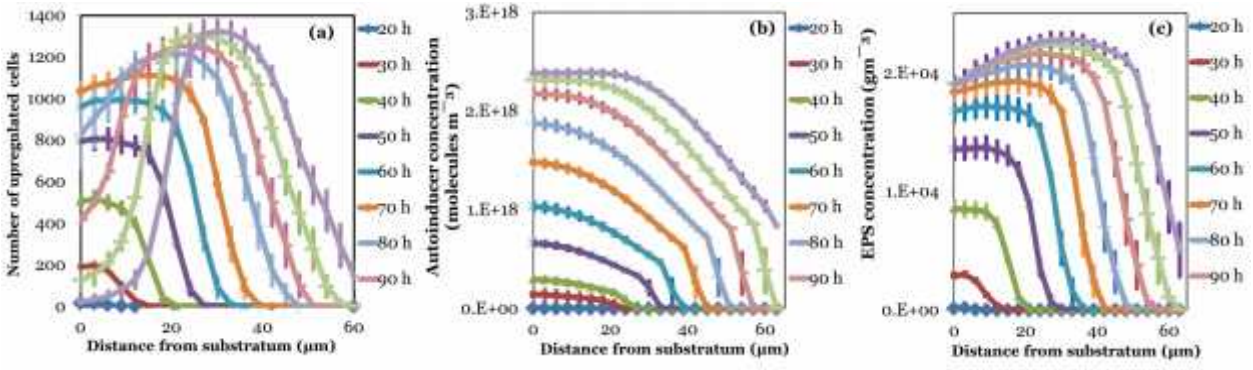

Fig. 8. Distribution of upregulated bacterial cells (a), and concentration distributions for the autoinducer (b) and EPS (c) for $C_{N,bulk}$ = 4 gm^{-3} for QS$^+$ biofilms. Data represent mean ± SEM for four separate simulations.

For biofilms utilizing QS, the number of upregulated cells increased with time (Fig. 8a), resulting in a corresponding increase in the average autoinducer (Fig. 8b) and EPS concentrations (Fig. 8c). Although the entire biofilm was primarily comprised of upregulated cells (Fig. 4a), maximal autoinducer and EPS concentrations occurred in the lower layers, and decreased farther away from the substratum (Figs. 8b, 8c). This could be explained as follows: nonuniform distribution of bacterial biomass results in spatially irregular rates of autoinducer production. Maximal autoinducer production occurs in the intermediate layers (with highest biomass concentrations), with production rates decreasing in the top and bottom layers. Thus, vertical autoinducer concentration gradients are set up, resulting in diffusion towards the DBL and the substratum. The no-flux boundary condition at the substratum results in the accumulation of the autoinducer in the lower region of the biofilm. On the other hand, the Dirichlet condition applied at the DBL causes the autoinducer in the top layers to be removed from the domain. In the stationary growth phase, although biomass density near the substratum was low, EPS concentrations were high and uniform. This is a consequence of the fact that EPS produced by cells prior to dying remains within the domain, causing EPS to accumulate in this part of the biofilm.

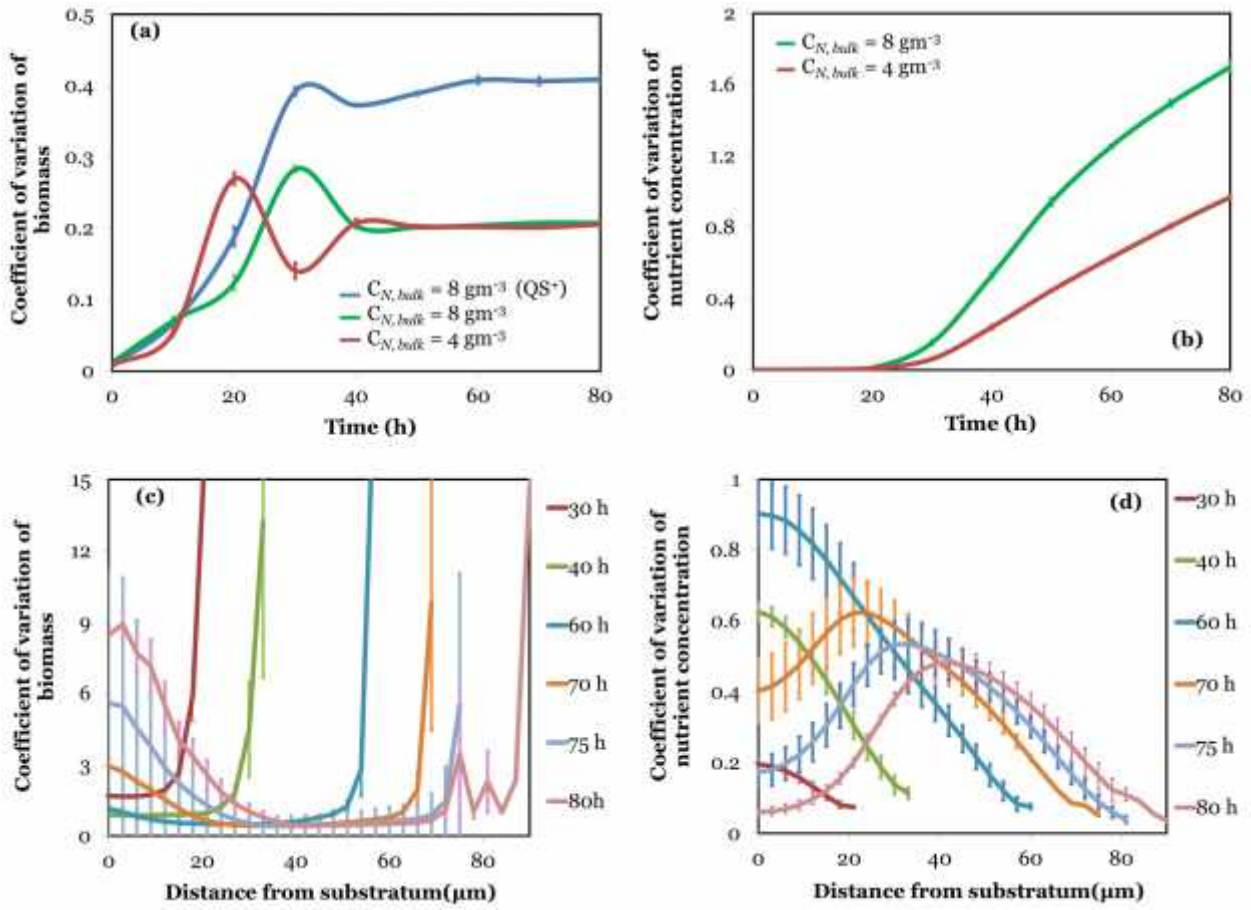

Fig. 9. Biofilm heterogeneity, expressed as the coefficients of variation for the biomass (a) and nutrient concentration (b), tracked over time under two nutrient conditions ($C_{N,bulk}$ = 8, 4 gm^{-3}); variation of heterogeneity in biomass (c) and nutrient concentration (d) as a function of the distance from the substratum; comparison of biomass heterogeneity for QS^+ and QS^- biofilms for $C_{N,bulk}$ = 8 gm^{-3} is shown in panel (a).

At the bulk nutrient concentration of 8 gm^{-3}, the overall biomass heterogeneity increased rapidly in the early exponential phase, and reached a maximum of 0.28 ± 0.004 at 30 h. As the biofilm developed further -- resulting in an increase in the number of mature cells -- a corresponding lowering of the overall biomass heterogeneity was observed. Heterogeneity remained virtually constant after 40 h of biofilm growth. A similar trend was observed for biofilms associated with the bulk nutrient concentration of 4 gm^{-3} (Fig. 9a). The QS^+ biofilm was more heterogeneous compared to the QS^- biofilm at all times tested (Fig. 9a). This could be a direct consequence of the nonuniform distribution of EPS in the QS^+ biofilm (Fig. 8c). In contrast, the coefficient of variation for the nutrient concentration increased monotonically with time in the exponential growth phase for both bulk nutrient concentrations studied (Fig. 9b). In the lag phase, nutrient concentration was homogeneous throughout the biofilm (Fig. 9b). In the early exponential growth phase nutrient heterogeneity was maximal in the lowermost layers (Fig. 9d). In the late exponential and stationary phases, maximal heterogeneity was observed in the intermediate layers

(Fig. 9d). This correlates with the observation that in the late exponential phase the proportion of biomass in the intermediate layers is maximal (Fig. 7a).

We next investigated the spatial variation of biofilm heterogeneity for the bulk nutrient concentration of 8 gm^{-3}. At low time points (upto 60 h), biofilm heterogeneity was low throughout the bulk of the biofilm, and was virtually independent of the distance from the substratum. The heterogeneity showed a marked increase near the DBL because of the stochastic nature of the cell division process in the top layers. Beyond 60 h, biofilm heterogeneity showed a significant increase in the lower layers (Fig. 9c). This is a consequence of the initiation of cell death events at the 60 h time point. At 80 h, the heterogeneity at the lowest layer reached a maximum (8.4 ± 0.4), resulting in sloughing of the biomass. Taken together, this analysis suggests that sloughing of the biofilm is a direct consequence of the increased biomass heterogeneity in the lower regions of the biofilm. The enhancement of the local heterogeneity near the substratum can be explained by the increased rates of cell death in this portion of the biofilm.

Conclusions

While it is well-known that biofilm-associated microorganisms are more tolerant to antibiotics compared to their planktonic counterparts, it is only subpopulations of cells that exhibit increased antibiotic resistances. However, the underlying biophysical mechanisms for the emergence of these antibiotic-insensitive subpopulations remain obscure. A systematic investigation of the spatiotemporal variation of structural and chemical heterogeneity in biofilms could aid in delineating mechanisms of antibiotic resistance at the fine scale. In this work, we used an individual-based cellular automata model to simulate biofilm growth under diverse nutrient conditions, in the presence and absence of quorum sensing. Each bacterium was modeled as an independent entity, allowing us to monitor structural and chemical heterogeneity of the biofilm as a function of time and space.

The key findings are summarized below:

1. Mature biofilms comprise of three structurally distinct layers: a highly porous homogeneous region sandwiched between two compact regions of high heterogeneity. This results in the formation of a mushroom-like structure with a low-density, high-volume "head," supported by a compact, low-volume "stalk" underneath.
2. Biofilms utilizing QS grow faster and are more heterogeneous compared to their QS^- counterparts. An additional layer of EPS -- devoid of cells -- forms atop the substratum, upon which the rest of the biofilm continues to develop. In agreement with experimental results, the model predicts that biofilms utilizing QS are structurally more stable, exhibiting a prolonged stationary growth phase, and a resistance to sloughing.
3. Whereas the biomass distribution is virtually uniform throughout the biofilm in the lag and early exponential growth phases, it undergoes a dramatic transformation in the late exponential and stationary phases with maximal biomass occurring in the middle layers of the biofilm. The heterogeneity and thickness of the lowermost layer increased with time, ultimately leading to sloughing. This is a direct consequence of preferential cell death occurring in close proximity to the substratum.
4. We were able to illustrate the formation of microcolonies comprising of metabolically inactive cells surrounded by cells exhibiting high growth rates. We hypothesize that these dormant cellular micro-compartments represent sites of low antibiotic susceptibility. There are two possible reasons for this: (i) the surrounding high-activity cell clusters may present a reaction-diffusion barrier, thereby decreasing antibiotic penetration to the microniches, and (ii) low-activity cells may consume antibiotics at a diminished rate, thereby reducing efficacy of treatment. A systematic investigation of the structural properties of these sections of the biofilm, and their response to antibiotic treatment may shed light on the biophysical mechanisms of antibiotic resistance.

In the future, we plan to use the current model to investigate the response of bacterial biofilms to antibiotic treatment. Since the model simulates spatiotemporal variability of biofilm constituents

(such as biomass, EPS, nutrient, and signaling molecules), it may be instructive to correlate antibiotic-resistant of bacterial biofilms with the emergence of metabolically inactive cell clusters.

Acknowledgments

This work was supported by the Start-Up Research Grant (No. SB/YS/LS-210/2013), Science and Engineering Research Board, India.

References

1. Hall-Stoodley, L., J.W. Costerton, and P. Stoodley, *Bacterial biofilms: from the natural environment to infectious diseases.* Nat Rev Microbiol, 2004. **2**(2): p. 95-108.
2. Ma, R., et al., *Modeling of diffusion transport through oral biofilms with the inverse problem method.* Int J Oral Sci, 2010. **2**(4): p. 190-7.
3. Stoodley, P., D. Debeer, and Z. Lewandowski, *Liquid flow in biofilm systems.* Appl Environ Microbiol, 1994. **60**(8): p. 2711-6.
4. Hunter, R.C. and T.J. Beveridge, *High-resolution visualization of Pseudomonas aeruginosa PAO1 biofilms by freeze-substitution transmission electron microscopy.* J Bacteriol, 2005. **187**(22): p. 7619-30.
5. Jefferson, K.K., D.A. Goldmann, and G.B. Pier, *Use of confocal microscopy to analyze the rate of vancomycin penetration through Staphylococcus aureus biofilms.* Antimicrob Agents Chemother, 2005. **49**(6): p. 2467-73.
6. Lawrence, J.R., et al., *Optical sectioning of microbial biofilms.* J Bacteriol, 1991. **173**(20): p. 6558-67.
7. Yang, X., et al., *Quantifying biofilm structure using image analysis.* J Microbiol Methods, 2000. **39**(2): p. 109-19.
8. Costerton, J.W., et al., *Bacterial biofilms in nature and disease.* Annu Rev Microbiol, 1987. **41**: p. 435-64.
9. Stoodley, P., et al., *Biofilms as complex differentiated communities.* Annu Rev Microbiol, 2002. **56**: p. 187-209.
10. Bassler, B.L., et al., *Intercellular signalling in Vibrio harveyi: sequence and function of genes regulating expression of luminescence.* Mol Microbiol, 1993. **9**(4): p. 773-86.
11. Matz, C., et al., *Microcolonies, quorum sensing and cytotoxicity determine the survival of Pseudomonas aeruginosa biofilms exposed to protozoan grazing.* Environ Microbiol, 2004. **6**(3): p. 218-26.
12. McDougald, D., et al., *Should we stay or should we go: mechanisms and ecological consequences for biofilm dispersal.* Nat Rev Microbiol, 2012. **10**(1): p. 39-50.
13. Stoodley, P., et al., *Influence of hydrodynamics and nutrients on biofilm structure.* J Appl Microbiol, 1998. **85 Suppl 1**: p. 19S-28S.
14. Potera, C., *Forging a link between biofilms and disease.* Science, 1999. **283**(5409): p. 1837, 1839.
15. Deretic, V., et al., *Conversion of Pseudomonas aeruginosa to mucoidy in cystic fibrosis: environmental stress and regulation of bacterial virulence by alternative sigma factors.* J Bacteriol, 1994. **176**(10): p. 2773-80.
16. Rayner, M.G., et al., *Evidence of bacterial metabolic activity in culture-negative otitis media with effusion.* JAMA, 1998. **279**(4): p. 296-9.
17. Blaser, J., et al., *In vivo verification of in vitro model of antibiotic treatment of device-related infection.* Antimicrob Agents Chemother, 1995. **39**(5): p. 1134-9.
18. Darouiche, R.O., et al., *Vancomycin penetration into biofilm covering infected prostheses and effect on bacteria.* J Infect Dis, 1994. **170**(3): p. 720-3.
19. Stickler, D.J., et al., *Biofilms on indwelling urethral catheters produce quorum-sensing signal molecules in situ and in vitro.* Appl Environ Microbiol, 1998. **64**(9): p. 3486-90.
20. Ward, K.H., et al., *Mechanism of persistent infection associated with peritoneal implants.* J Med Microbiol, 1992. **36**(6): p. 406-13.
21. Gefen, O. and N.Q. Balaban, *The importance of being persistent: heterogeneity of bacterial populations under antibiotic stress.* FEMS Microbiol Rev, 2009. **33**(4): p. 704-17.

22. Gefen, O., et al., *Single-cell protein induction dynamics reveals a period of vulnerability to antibiotics in persister bacteria.* Proc Natl Acad Sci U S A, 2008. **105**(16): p. 6145-9.
23. Keren, I., et al., *Specialized persister cells and the mechanism of multidrug tolerance in Escherichia coli.* J Bacteriol, 2004. **186**(24): p. 8172-80.
24. Keren, I., et al., *Persister cells and tolerance to antimicrobials.* FEMS Microbiol Lett, 2004. **230**(1): p. 13-8.
25. Kussell, E., et al., *Bacterial persistence: a model of survival in changing environments.* Genetics, 2005. **169**(4): p. 1807-14.
26. Mulcahy, L.R., et al., *Emergence of Pseudomonas aeruginosa strains producing high levels of persister cells in patients with cystic fibrosis.* J Bacteriol, 2010. **192**(23): p. 6191-9.
27. Stewart, P.S. and M.J. Franklin, *Physiological heterogeneity in biofilms.* Nat Rev Micro, 2008. **6**(3): p. 199-210.
28. Queck, S.Y., et al., *RNAIII-independent target gene control by the agr quorum-sensing system: insight into the evolution of virulence regulation in Staphylococcus aureus.* Mol Cell, 2008. **32**(1): p. 150-8.
29. Pu, Y., et al., *Enhanced Efflux Activity Facilitates Drug Tolerance in Dormant Bacterial Cells.* Mol Cell, 2016. **62**(2): p. 284-94.
30. De Beer, D., R. Srinivasan, and P.S. Stewart, *Direct measurement of chlorine penetration into biofilms during disinfection.* Appl Environ Microbiol, 1994. **60**(12): p. 4339-44.
31. Grobe, K.J., J. Zahller, and P.S. Stewart, *Role of dose concentration in biocide efficacy against Pseudomonas aeruginosa biofilms.* J Ind Microbiol Biotechnol, 2002. **29**(1): p. 10-5.
32. Ng, W.L. and B.L. Bassler, *Bacterial quorum-sensing network architectures.* Annu Rev Genet, 2009. **43**: p. 197-222.
33. Rutherford, S.T. and B.L. Bassler, *Bacterial quorum sensing: its role in virulence and possibilities for its control.* Cold Spring Harb Perspect Med, 2012. **2**(11).
34. Fuqua, C. and E.P. Greenberg, *Listening in on bacteria: acyl-homoserine lactone signalling.* Nat Rev Mol Cell Biol, 2002. **3**(9): p. 685-95.
35. Davies, D.G., et al., *The involvement of cell-to-cell signals in the development of a bacterial biofilm.* Science, 1998. **280**(5361): p. 295-8.
36. Quinones, B., G. Dulla, and S.E. Lindow, *Quorum sensing regulates exopolysaccharide production, motility, and virulence in Pseudomonas syringae.* Mol Plant Microbe Interact, 2005. **18**(7): p. 682-93.
37. Koutsoudis, M.D., et al., *Quorum-sensing regulation governs bacterial adhesion, biofilm development, and host colonization in Pantoea stewartii subspecies stewartii.* Proc Natl Acad Sci U S A, 2006. **103**(15): p. 5983-8.
38. von Bodman, S.B., D.R. Majerczak, and D.L. Coplin, *A negative regulator mediates quorum-sensing control of exopolysaccharide production in Pantoea stewartii subsp. stewartii.* Proc Natl Acad Sci U S A, 1998. **95**(13): p. 7687-92.
39. Tan, C.H., et al., *The role of quorum sensing signalling in EPS production and the assembly of a sludge community into aerobic granules.* ISME J, 2014. **8**(6): p. 1186-97.
40. Frederick, M.R., et al., *A mathematical model of quorum sensing regulated EPS production in biofilm communities.* Theor Biol Med Model, 2011. **8**: p. 8.
41. Boyd, A. and A.M. Chakrabarty, *Role of alginate lyase in cell detachment of Pseudomonas aeruginosa.* Appl Environ Microbiol, 1994. **60**(7): p. 2355-9.
42. Janissen, R., et al., *Spatiotemporal distribution of different extracellular polymeric substances and filamentation mediate Xylella fastidiosa adhesion and biofilm formation.* Sci Rep, 2015. **5**: p. 9856.

43. Ma, L., et al., *Assembly and development of the Pseudomonas aeruginosa biofilm matrix.* PLoS Pathog, 2009. **5**(3): p. e1000354.
44. Tseng, B.S., et al., *The extracellular matrix protects Pseudomonas aeruginosa biofilms by limiting the penetration of tobramycin.* Environ Microbiol, 2013. **15**(10): p. 2865-78.
45. Lewis, K., *Persister cells, dormancy and infectious disease.* Nat Rev Microbiol, 2007. **5**(1): p. 48-56.
46. Jayaraman, A. and T.K. Wood, *Bacterial quorum sensing: signals, circuits, and implications for biofilms and disease.* Annu Rev Biomed Eng, 2008. **10**: p. 145-67.
47. Alpkvist, E. and I. Klapper, *A multidimensional multispecies continuum model for heterogeneous biofilm development.* Bull Math Biol, 2007. **69**(2): p. 765-89.
48. Duddu, R., D.L. Chopp, and B. Moran, *A two-dimensional continuum model of biofilm growth incorporating fluid flow and shear stress based detachment.* Biotechnol Bioeng, 2009. **103**(1): p. 92-104.
49. Kreft, J.U., et al., *Individual-based modelling of biofilms.* Microbiology, 2001. **147**(Pt 11): p. 2897-912.
50. Emerenini, B.O., et al., *A Mathematical Model of Quorum Sensing Induced Biofilm Detachment.* PLoS One, 2015. **10**(7): p. e0132385.
51. Fozard, J.A., et al., *Inhibition of quorum sensing in a computational biofilm simulation.* Biosystems, 2012. **109**(2): p. 105-14.
52. Langebrake, J.B., et al., *Traveling waves in response to a diffusing quorum sensing signal in spatially-extended bacterial colonies.* J Theor Biol, 2014. **363**: p. 53-61.
53. Anguige, K., J.R. King, and J.P. Ward, *Modelling antibiotic- and anti-quorum sensing treatment of a spatially-structured Pseudomonas aeruginosa population.* J Math Biol, 2005. **51**(5): p. 557-94.
54. Wanner, O. and W. Gujer, *A multispecies biofilm model.* Biotechnol Bioeng, 1986. **28**(3): p. 314-28.
55. Klapper, I. and J. Dockery, *Finger Formation in Biofilm Layers.* SIAM Journal on Applied Mathematics, 2002. **62**(3): p. 853-869.
56. Alpkvist, E., et al., *Three-dimensional biofilm model with individual cells and continuum EPS matrix.* Biotechnol Bioeng, 2006. **94**(5): p. 961-79.
57. Chambless, J.D., S.M. Hunt, and P.S. Stewart, *A three-dimensional computer model of four hypothetical mechanisms protecting biofilms from antimicrobials.* Appl Environ Microbiol, 2006. **72**(3): p. 2005-13.
58. Picioreanu, C., J.U. Kreft, and M.C. Van Loosdrecht, *Particle-based multidimensional multispecies biofilm model.* Appl Environ Microbiol, 2004. **70**(5): p. 3024-40.
59. Kreft, J.U. and J.W. Wimpenny, *Effect of EPS on biofilm structure and function as revealed by an individual-based model of biofilm growth.* Water Sci Technol, 2001. **43**(6): p. 135-41.
60. Fagerlind, M.G., et al., *Dynamic modelling of cell death during biofilm development.* J Theor Biol, 2012. **295**: p. 23-36.
61. Chang, I., et al., *A three-dimensional, stochastic simulation of biofilm growth and transport-related factors that affect structure.* Microbiology, 2003. **149**(Pt 10): p. 2859-71.
62. Picioreanu, C., M.C. Van Loosdrecht, and J.J. Heijnen, *Effect of diffusive and convective substrate transport on biofilm structure formation: a two-dimensional modeling study.* Biotechnol Bioeng, 2000. **69**(5): p. 504-15.
63. Eberl H, M.E., Noguera D, Picioreanu C, Rittmann B, van Loosdrecht M, Wanner O *Mathematical modeling of biofilms.* IWA Publishing, 2006.
64. Castro, S.L., et al., *Induction of attachment-independent biofilm formation and repression of Hfq expression by low-fluid-shear culture of Staphylococcus aureus.* Appl Environ Microbiol, 2011. **77**(18): p. 6368-78.

65. Guo, P., A.M. Weinstein, and S. Weinbaum, *A hydrodynamic mechanosensory hypothesis for brush border microvilli.* Am J Physiol Renal Physiol, 2000. **279**(4): p. F698-712.
66. Ardre, M., et al., *An individual-based model for biofilm formation at liquid surfaces.* Phys Biol, 2015. **12**(6): p. 066015.
67. Kreft, J.U., G. Booth, and J.W. Wimpenny, *BacSim, a simulator for individual-based modelling of bacterial colony growth.* Microbiology, 1998. **144 (Pt 12)**: p. 3275-87.
68. Picioreanu, C., M.C. van Loosdrecht, and J.J. Heijnen, *Mathematical modeling of biofilm structure with a hybrid differential-discrete cellular automaton approach.* Biotechnol Bioeng, 1998. **58**(1): p. 101-16.
69. Picioreanu, C., M.C. van Loosdrecht, and J.J. Heijnen, *A new combined differential-discrete cellular automaton approach for biofilm modeling: application for growth in gel beads.* Biotechnol Bioeng, 1998. **57**(6): p. 718-31.
70. Hunt, S.M., et al., *Hypothesis for the role of nutrient starvation in biofilm detachment.* Appl Environ Microbiol, 2004. **70**(12): p. 7418-25.
71. Nystrom, T., *Not quite dead enough: on bacterial life, culturability, senescence, and death.* Arch Microbiol, 2001. **176**(3): p. 159-64.
72. Nystrom, T., *Conditional senescence in bacteria: death of the immortals.* Mol Microbiol, 2003. **48**(1): p. 17-23.
73. Postgate, J.R. and J.R. Hunter, *The survival of starved bacteria.* J Gen Microbiol, 1962. **29**: p. 233-63.
74. Chambless, J.D. and P.S. Stewart, *A three-dimensional computer model analysis of three hypothetical biofilm detachment mechanisms.* Biotechnol Bioeng, 2007. **97**(6): p. 1573-84.
75. Picioreanu, C., M.C. van Loosdrecht, and J.J. Heijnen, *Two-dimensional model of biofilm detachment caused by internal stress from liquid flow.* Biotechnol Bioeng, 2001. **72**(2): p. 205-18.
76. Stewart, P.S., *A model of biofilm detachment.* Biotechnol Bioeng, 1993. **41**(1): p. 111-7.
77. Pizarro, G.E., et al., *Two-dimensional cellular automaton model for mixed-culture biofilm.* Water Sci Technol, 2004. **49**(11-12): p. 193-8.
78. Falsetta, M.L., et al., *Symbiotic relationship between Streptococcus mutans and Candida albicans synergizes virulence of plaque biofilms in vivo.* Infect Immun, 2014. **82**(5): p. 1968-81.
79. Leisner, M., et al., *Kinetics of genetic switching into the state of bacterial competence.* Biophys J, 2009. **96**(3): p. 1178-88.
80. Koerber, A.J., et al., *A mathematical model of partial-thickness burn-wound infection by Pseudomonas aeruginosa: quorum sensing and the build-up to invasion.* Bull Math Biol, 2002. **64**(2): p. 239-59.
81. Bester, E., et al., *Planktonic-cell yield of a pseudomonad biofilm.* Appl Environ Microbiol, 2005. **71**(12): p. 7792-8.
82. Kroukamp, O., R.G. Dumitrache, and G.M. Wolfaardt, *Pronounced effect of the nature of the inoculum on biofilm development in flow systems.* Appl Environ Microbiol, 2010. **76**(18): p. 6025-31.
83. Rochex, A. and J.M. Lebeault, *Effects of nutrients on biofilm formation and detachment of a Pseudomonas putida strain isolated from a paper machine.* Water Res, 2007. **41**(13): p. 2885-92.